Extended theoretical modeling of reverse intersystem crossing for thermally activated delayed fluorescence materials

Masaya Hagai[1*], Naoto Inai[1], Takuma Yasuda[2,3*], Kazuhiro J. Fujimoto[1,4*] and Takeshi Yanai[1,4*]

[1]Department of Chemistry, Graduate School of Science and Integrated Research Consortium on Chemical Science (IRCCS), Nagoya University, Furo-cho, Chikusa-ku, Nagoya, 464-8601, Aichi, Japan.

[2]Institute for Advanced Study, Kyushu University, 744 Motooka, Nishi-ku, Fukuoka, 819-0395, Kyushu, Japan.

[3]Department of Applied Chemistry, Graduate School of Engineering, Kyushu University, 744 Motooka, Nishi-ku, Fukuoka, 819-0395, Kyushu, Japan.

[4]Institute of Transformative Bio-Molecules (WPI-ITbM), Nagoya University, Furo-cho, Chikusa-ku, Nagoya, 464-8601, Aichi, Japan.

*Corresponding author(s). E-mail(s): hagai.masaya.v9@s.mail.nagoya-u.ac.jp; yasuda@ifrc.kyushu-u.ac.jp; fujimotok@chem.nagoya-u.ac.jp; yanait@gmail.com;

Contributing authors: inai.qcg@gmail.com;

Abstract

Thermally activated delayed fluorescence (TADF) materials and multi-resonant (MR) variants are promising organic emitters that can achieve an internal electroluminescence quantum efficiency of approximately 100%. The reverse intersystem crossing (RISC) is key for harnessing triplet energies for fluorescence. Theoretical modeling is thus crucial to estimate its rate constant (k_{RISC}) for material development. Herein, we present a comprehensive assessment of the theory for simulating the RISC of MR-TADF molecules within a perturbative excited-state dynamics framework. Our extended rate formula reveals the importance of the concerted effects of nonadiabatic spin-vibronic coupling and vibrationally induced spin-orbital couplings in reliably determining k_{RISC} of MR-TADF molecules. The excited singlet-triplet energy gap is another factor influencing k_{RISC}. We present a new scheme for gap estimation using experimental Arrhenius plots of k_{RISC}. Erroneous behavior caused by approximations in Marcus theory is elucidated by testing 121 MR-TADF molecules. Our extended modeling offers in-depth descriptions of k_{RISC}. ($\lesssim$150 words)

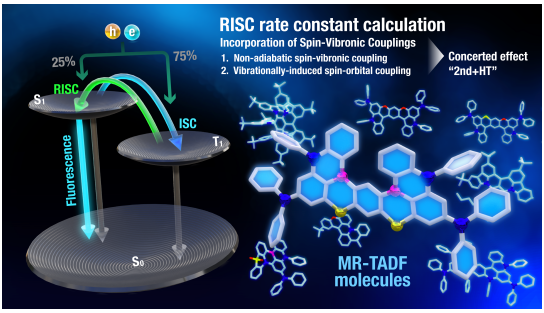

Keywords: Multi-Resonance Thermally Activated Delayed Fluorescence, Reverse Intersystem Crossing, Thermal Vibration Correlation Function Theory, Spin Vibronic Coupling,

1 Introduction

Organic light-emitting diodes (OLEDs) [1] have gained widespread interest owing to their remarkable features such as lightness and wide viewing range. Materials that emit light through fluorescence [2, 3] and phosphorescence [4–6] have been developed for their application in OLEDs. Electrical excitations that occur in OLED devices produce singlet and triplet excitons in a ratio of 1:3 through hole-electron recombination [4]. To increase the internal quantum efficiency (IQE) to ∼100%, all generated excitons with different spin multiplicities have to be used for electroluminescence. To meet this demand, Adachi et al. developed OLEDs based on thermally activated delayed fluorescence (TADF) [7]. TADF is a process in which a non-radiative triplet exciton is converted into a radiative singlet exciton *via* reverse intersystem crossing (RISC), followed by delayed fluorescence (Fig. 1**a**). TADF materials show significant potential for fully utilizing singlet and triplet excitons for fluorescence; materials have been reported to achieve nearly 100% IQE [8–10]. Recently, TADF coupled with the multiple resonance (MR) effect, designated MR-TADF [11], has received considerable attention as synthesized MR-TADF luminophores demonstrate desirable narrowband emissions with high IQE and color purity [12–14].

A large spin-orbit coupling (SOC) and small adiabatic singlet-triplet (ST) energy difference ΔE_{ST} are important physical factors for accelerating the rate-limiting RISC process. Theoretical modeling will assist in characterizing details of the RISC process and realizing chemical fine-tuning. The semiclassical Marcus formula [15] has been conventionally used to estimate the rate constant k_{RISC} and can describe state-transition processes based on ΔE_{ST} and SOC [16–19]. Recent studies have shown that the effects of spin-vibronic coupling (SVC) [20–28], which are discarded in Marcus theory, are impactful to tuning k_{RISC} for TADF molecules [24, 25, 29, 30]. Two types of SVC impact the predicted value of k_{RISC}. The first is expressed through Fermi's golden rule as the second-order vibronic perturbation term [20–25] and is hereafter referred to as nonadiabatic SVC (NA-SVC). It is caused by the interplay between nonadiabatic coupling (NAC) and SOC. The second is the vibrationally induced SOC, which is related to the first derivatives of the SOC [20, 26–28, 30]. This effect is called Herzberg–Teller SVC (HT-SVC).

Several previous studies [21–25] have confirmed that the NA-SVC effect can significantly enhance k_{RISC} by several orders of magnitude through indirect spin-flipping mediated by intermediate excited states such as T_2 and T_3. Moreover, the HT-SVC effect coupled with spin conversion is considered crucial for further influencing k_{RISC}. Marian et al. investigated critical effects of HT-SVC on spin-flipping processes [20, 26–28, 30]. A recent study revealed that the simulated k_{RISC} for MR-TADF emitters could increase by more than one order of magnitude when incorporating HT-SVC into the rate formula

[29]. The derived formula was based on the direct sum of the individual rate contributions associated with the NA-SVC and HT-SVC separately. To the best of our knowledge, no existing rate formula considers the fully concerted coupling of both effects. Developing such a formula could help capture additional RISC channels opened by the HT-SVC effects coupled with the indirect spin-flipping process through low-lying intermediate T_n states (Fig. 1**b**).

The accuracy of ΔE_{ST} is crucial because k_{RISC} steeply varies depending on ΔE_{ST}, as in Marcus theory. There are two types of experimental approaches for measuring ΔE_{ST}: (1) fluorescence and phosphorescence energy difference and (2) activation energy of the RISC process [31]. In the latter, the activation energy E_a^{Exp} is determined from the slope of the Arrhenius plot of the measured k_{RISC} versus temperature T using the Arrhenius equation $\ln k = -\frac{E_a}{k_{\mathrm{B}}T} + \ln A$. E_a^{Exp} is then interpreted as ΔE_{ST} [7, 31]. Computational quantum chemical approaches to gauge ΔE_{ST} should be an effective alternative; however, there are uncontrollable difficulties in reliably predicting small ΔE_{ST} for TADF molecules using the time-dependent density-functional theory (TDDFT). More computationally demanding treatments involving correlated wave function theories have been shown to mitigate these challenges [32–34].

In this study, we aimed to elucidate in-depth aspects of the theory for simulating k_{RISC} for MR-TADF materials. A simplified excited-state dynamics approach is desirable for MR-TADF molecules with large π-conjugated systems. Thus, a perturbative treatment based on Fermi's golden rule was considered. Additionally, for their construction, the electronic-state potential energy surfaces were assumed to be harmonic in all dimensions. To facilitate formulation and computation, the thermal vibration correlation function (TVCF) formalism [21, 35] was employed. Our major interest was to investigate the influence of the treatment of NA-SVC and HT-SVC and their concerted effects on k_{RISC}. This fully concerted SVC effect is denoted 2nd+HT (Fig. 1**b**). We developed an enhanced TVCF-based method considering the 2nd+HT effect (Sec. S7). Furthermore, we investigated the choice of ΔE_{ST}, which can be determined using experimental data or quantum chemical computations. We also introduced a novel approach for estimating ΔE_{ST} based on fitting the experimental Arrhenius plots. Additionally, the reliability of Marcus theory was assessed by contrasting TVCF predictions for 121 MR-TADF molecules. We discussed approximation errors in Marcus theory.

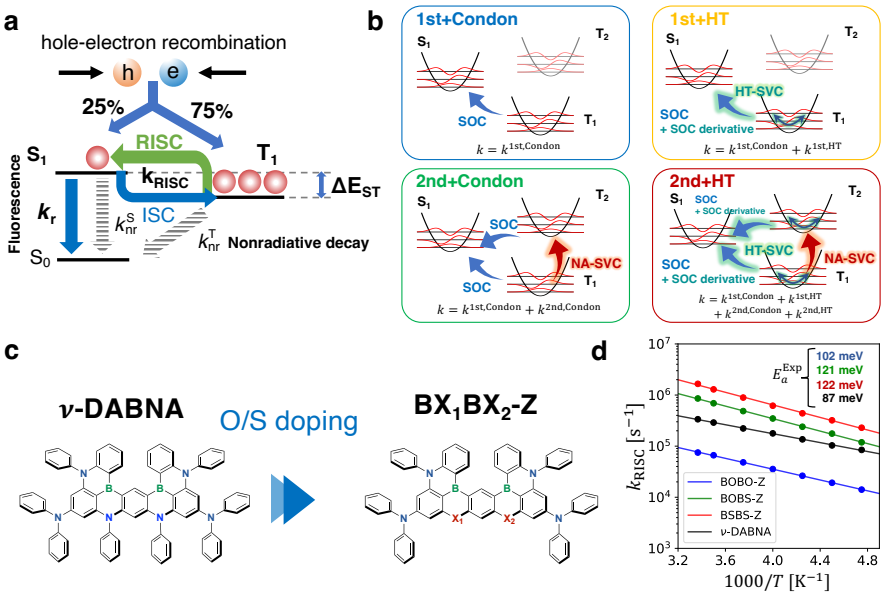

Fig. 1 a, Conceptual diagram of TADF process. **b,** Treatments of RISC process using 1st+Condon, 2nd+Condon, 1st+HT, and 2nd+HT TVCF methods. Compared to the 1st method, the 2nd approach additionally accounts for NA-SVC. The HT treatment considers HT-SVC, which is discarded by the Condon treatment. **c,** ν-DABNA, BOBO-Z (X_1=X_2=O), BOBS-Z (X_1=O, X_2=S), and BSBS-Z (X_1=X_2=S). **d,** Arrhenius plots and activation energies E_a^{Exp} obtained using the relation $\ln k_{\mathrm{RISC}} = -E_a^{\mathrm{Exp}}/(k_{\mathrm{B}}T) + \ln A$.

2 Results and discussion

2.1 Calculation of RISC rate constant using experimental E_a^{Exp} as ΔE_{ST}

ν-DABNA [36] and its element-substituted analogs, BOBO-Z, BOBS-Z, and BSBS-Z [37], are state-of-the-art MR-TADF materials with narrowband blue emissions (Fig. 1**c**). We performed k_{RISC} calculations on these compounds as test cases. We assessed the predictions of the four levels of the TVCF theory, termed as 1st+Condon, 2nd+Condon, 1st+HT, and 2nd+HT (Fig. 1**b**; see Methods), and Marcus theory. The rate equations of all these theories commonly form as a function of ΔE_{ST} and T. The ΔE_{ST} can be considered a free parameter. We set ΔE_{ST} to the measured E_a^{Exp} corresponding to the slope of the experimental Arrhenius plots (Fig. 1**d**) and T to 300 K. TVCF simulation requires harmonic vibrational wave functions, which were computed at the DFT level. The results are shown in Figs. 2**a** and 2**b** (see also Table S1).

Figs. 2**a** and 2**b** show that, overall, the 2nd+Condon and 1st+HT methods predicted larger k_{RISC} values than the 1st+Condon method, showing good

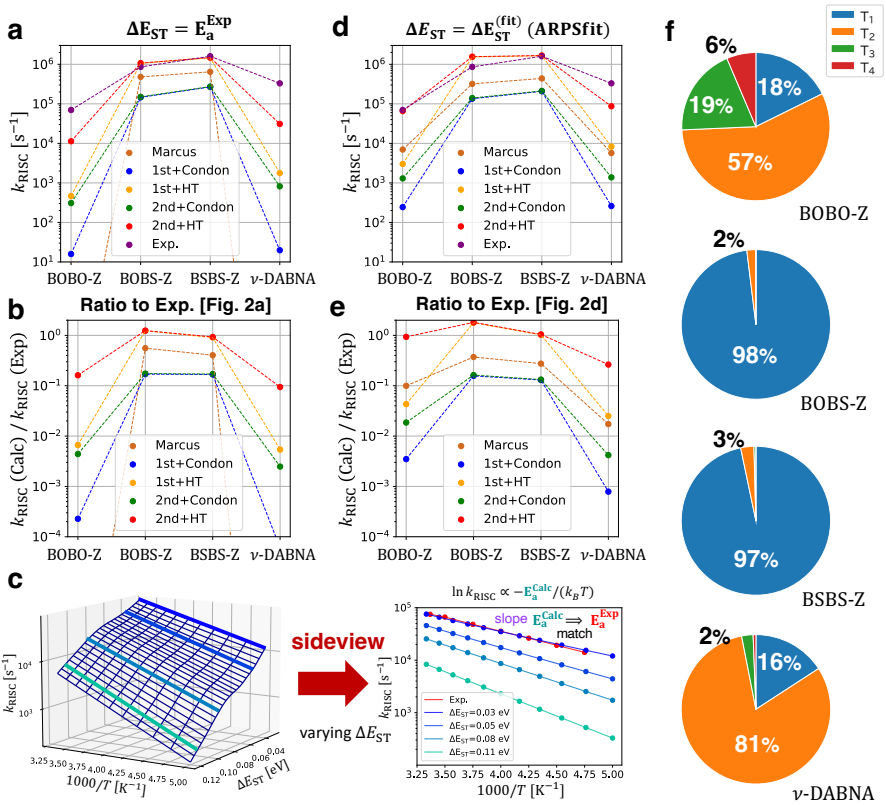

Fig. 2 **a,b,** k_{RISC} calculated by various rate constant formulas using E_a^{Exp} as ΔE_{ST}, and the ratio of the predicted k_{RISC} to the experimental value for BXBX-Z and ν-DABNA. **c,** Overview of the Arrhenius plot slope fitting (ARPSfit) method to determine $\Delta E_{ST}^{(fit)}$ with which the rate constant calculation can reproduce the experimental Arrhenius plot with its slope E_a^{Exp}. **d,e,** k_{RISC} calculated by various rate constant formulas using $\Delta E_{ST}^{(fit)}$ obtained by the ARPSfit method, and the ratio of the predicted k_{RISC} to the experimental value. **f,** Contributions of the direct process (T_1) and indirect processes mediated by the intermediate states, T_2, T_3, and T_4, to k_{RISC}.

agreement with the experimental values. This result indicates that considering either the NA-SVC or HT-SVC effects substantially improves the accuracy. The 2nd+HT model, considering both effects, provided the most accurate results within one order of magnitude of error relative to the experimental values. A comparison of the 1st+Condon and 1st+HT results revealed that k_{RISC} was remarkably increased by the HT-SVC effect itself by a factor of ten to a thousand. The notable differences between the 1st+HT and 2nd+HT predictions confirmed the importance of the NA-SVC effect, which was most pronounced in BOBO-Z and ν-DABNA. The impact was not significant for either BOBS-Z or BSBS-Z. The former feature could be explained by the fact that $\Delta E_{T_1T_2}$ was small (see also Sec. S2). Although the 2nd+HT model showed promising improvements, there were cases where it still performed

poorly; BOBO-Z and ν-DABNA showed unsatisfactory degrees of error. We speculated that these errors arose from the condition that ΔE_{ST} was set to E_a^{Exp}. This setup for ΔE_{ST} was employed in Refs. [7, 31].

2.2 Calculation of RISC rate constant calculation using ΔE_{ST} obtained by the slope fitting method

The observation in Sec. 2.1 prompted us to explore an alternative strategy to define the relationship between the experimental E_a^{Exp} and parameter ΔE_{ST} in the rate equations. The core of our new scheme designated "Arrhenius plot slope fitting (ARPSfit)" is computationally simulating the Arrhenius plots by evaluating the rate equation as a function of $1/T$ for a given ΔE_{ST}. Let the slope of the simulated Arrhenius plots be denoted E_a^{Calc}, which varies depending on the given value of ΔE_{ST} (Fig. 2**c**). In the ARPSfit method, the objective value of ΔE_{ST} is determined such that the associated E_a^{Calc} matches the preknowledge E_a^{Exp}. The ΔE_{ST} provided by the ARPSfit method is hereafter denoted $\Delta E_{\mathrm{ST}}^{(\mathrm{fit})}$ (Fig. 2**c**). To obtain a set of Arrhenius plots, the TVCF (or Marcus) formula was evaluated at eleven points of T in the range 200–300 K. Note that ARPSfit coupled with TVCF requires harmonic vibrational analysis.

The resulting $\Delta E_{\mathrm{ST}}^{(\mathrm{fit})}$ for the MR-TADF systems are summarized in Table S3. The $E_{\mathrm{ST}}^{(\mathrm{fit})}$ for BOBO-Z and ν-DABNA were predicted to be 0.035 and 0.037 eV, respectively, at the 2nd+HT TVCF level, which were smaller than the corresponding E_a^{Exp}, 0.102 and 0.087 eV, respectively. By substituting $\Delta E_{\mathrm{ST}}^{(\mathrm{fit})}$ into the rate equations, we re-evaluated k_{RISC} (Figs. 2**d** and 2**e**; Table S4). A comparison between Figs. 2**a** and 2**d** (or Figs. 2**b** and 2**e**) enabled us to examine the influence of the redefined ΔE_{ST} on k_{RISC}. Clearly, the use of the ARPSfit-based $\Delta E_{\mathrm{ST}}^{(\mathrm{fit})}$ effectively refined the RISC rate constant predictions for all cases compared to those obtained with the previous setting $\Delta E_{\mathrm{ST}} = E_a^{\mathrm{Exp}}$. Significant improvements were observed in the Marcus results. These results demonstrated that the ARPSfit method offered a marked improvement in determining ΔE_{ST} from E_a^{Exp}.

As observed in Sec. 2.1, the NA-SVC contribution appears to be prominent for BOBO-Z and ν-DABNA. To obtain detailed insights, we dissected k_{RISC} into state-wise contributions (Fig. 2**f**). Details of this analysis are presented in Sec. S2.2. The RISC transition for BOBS-Z and BSBS-Z was 97% or more, characterized as a direct $T_1 \rightarrow S_1$ process and almost unaffected by NA-SVC treatment. Conversely, a strong NA-SVC effect arose in BOBO-Z, in which the intermediate T_2 and T_3 states made large contributions *via* NA-SVC. Similarly, for ν-DABNA, the T_2-mediated NA-SVC channel accelerated the RISC process by a factor of 6.3, relative to the 1st+Condon/HT prediction. Importantly, Fig. 2**e** indicates that treatment at the 2nd+HT level was necessary to

quantitatively predict k_{RISC}. This indicates that the NA-SVC and HT-SVC effects manifested in the intermediate T_n states are adequately coupled. Surprisingly, the Marcus predictions were significantly improved using $\Delta E_{\mathrm{ST}}^{(\mathrm{fit})}$, closely approaching the experimental values, even for molecules where the NA-SVC effect discarded in Marcus formula was relevant. Sec. S3 discusses the first-principles calculations of ΔE_{ST} along with the k_{RISC} predictions using these ΔE_{ST}.

2.3 Comparison of 1st+Condon TVCF and semi-classical Marcus formula

The Marcus results provided relatively good accuracy and better agreement with the experimental values than the 1st+Condon predictions (Figs. 2**d** and 2**e**). This is remarkable because it contradicts the theoretical construction. Marcus formula corresponds to a model downgraded from the 1st+Condon theory. As discussed in Sec. 4.3, the relationship between the two models is clearly formulated through four approximation steps [38]: (1) Duschinsky rotation cutoff (Dus-off), (2) displaced harmonic oscillator (DHO), (3) short-time (st), and (4) high-temperature (ht) approximations. These procedures result in five hierarchical levels of rate-constant equations (Fig. 3**a**).

To determine why the Marcus model yielded such remarkable results, we numerically examined how these approximations affected the k_{RISC} computation. Here let us focus on BOBO-Z. The results for the other molecules are presented in Sec. S4. Fig. 3**b** shows the real part of the correlation functions $\rho(t)$ [equation (10)] at individual levels (e.g., equation (19b)). Applying a Fourier transform to these equations [equation (8)] yields k_{RISC} (e.g., equation (19a)), the values of which are displayed as a function of ΔE_{ST} in Fig. 3**c**. In this plot, the k_{RISC} values at a specific $\Delta E_{\mathrm{ST}}^{(\mathrm{fit})}$ (0.045 eV) for ΔE_{ST} can be seen. Monitoring these values revealed that the DHO and st approximations significantly affected k_{RISC} prediction.

Fig. 3**b** illustrates that the DHO approximation changes $\mathrm{Re}[\rho(t)]$ from the 1st+Condon's oscillatory damped shape to a monotonically decaying curve. Equation (8) can be reduced to the identity $k_{\mathrm{RISC}}\big|_{\Delta E_{\mathrm{ST}}=0} = \int_{-\infty}^{\infty} dt\, \mathrm{Re}[\rho(t)]$, indicating that it corresponds to the area of the region bounded by the curve $\mathrm{Re}[\rho(t)]$ in Fig. 3**b** (which appears as the intercepts of the curves plotted in Fig. 3**c**). Moreover, the DHO-approximated $k_{\mathrm{RISC}}\big|_{\Delta E_{\mathrm{ST}}=0}$ attains the largest value and is overestimated compared with the 1st+Condon counterpart. This trend reflects the fact that at the DHO level, $\mathrm{Re}[\rho(t)]$ is a positive function, while the 1st+Condon curve involves a positive-negative oscillation, which causes large-scale cancellation in its integration. The above analysis confirms that the DHO treatment spuriously increases k_{RISC}.

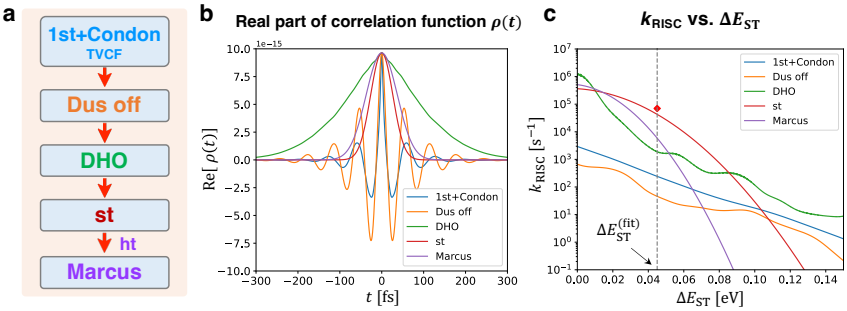

Fig. 3 a, Five hierarchical levels of the rate constant equations, 1st+Condon TVCF, Duschinsky rotation cutoff (Dus-off), displaced harmonic oscillator (DHO), and short-time (st) approximated models, and Marcus theory from high-temperature (ht) approximation. **b,** Plots of the real part of the correlation functions $\mathrm{Re}[\rho(t)]$ as a function of the time t evaluated at five levels of the theory for BOBO-Z. **c,** Plots of k_{RISC} as a function of E_{ST} evaluated at five levels of the theory for BOBO-Z. The gray vertical dashed line indicates the ARPSfit-based $\Delta E_{\mathrm{ST}}^{(\mathrm{fit})}$ determined at 1st+HT TVCF level. The red dot is the experimental value of k_{RISC}.

The Dus-off and DHO approximations to the 1st+Condon equation result in the following DHO-level expression:

$$k_{\mathrm{RISC}}^{\mathrm{DHO}}(\Delta E_{\mathrm{ST}}) = \frac{\left|H_{fi}^{\mathrm{SOC}}\right|^2}{\hbar^2} \int_{-\infty}^{\infty} dt\, e^{i\Delta E_{\mathrm{ST}}\, t/\hbar}\, \rho^{\mathrm{DHO}}(t)\,, \tag{1a}$$

$$\rho^{\mathrm{DHO}}(t) = \exp\left\{ -\sum_{j}^{N} S_j \Big[(1+2\bar{n}_j)(1-\cos(\omega_j t)) + i\sin(\omega_j t) \Big] \right\}, \tag{1b}$$

where the definitions of S_j, $\bar{n}_j$, and ω_j are given in Sec. 4.3. Applying the st approximation, equation 1 is reduced to

$$k_{\mathrm{RISC}}^{\mathrm{st}}(\Delta E_{\mathrm{ST}}) = \frac{\left|H_{fi}^{\mathrm{SOC}}\right|^2}{\hbar^2} \int_{-\infty}^{\infty} dt\, e^{i\left(\Delta E_{\mathrm{ST}} - \hbar\sum_j^N S_j\omega_j\right) t/\hbar}\, \rho^{\mathrm{st}}(t)\,, \tag{2a}$$

$$\rho^{\mathrm{st}}(t) = \exp\left\{ -\sum_{j}^{N} S_j \Big[(\bar{n}_j + 1/2)\, \omega_j^2 \Big]\, t^2 \right\}. \tag{2b}$$

The above analyses show that the st approximation transforms $\rho(t)$ into a Gaussian shape. Its Fourier transform [equation (2)] retains a Gaussian structure, as confirmed by the resulting st- and Marcus-level k_{RISC} curves (Fig. 3**c**). These curves exhibit negative quadratic decay on a logarithmic scale ($O(-\Delta E_{\mathrm{ST}}^2)$). With small ΔE_{ST}, this shape thus plays a role in artificially enlarging k_{RISC} with a slow decay, compared to a monotonic ($O(-\Delta E_{\mathrm{ST}})$) decay. Meanwhile, with larger ΔE_{ST}, the decay becomes increasingly steep and causes a near-diminishing k_{RISC}. Therefore, the favorable features of the

Marcus results for the four MR-TADF systems are fortuitous owing to error cancellation.

2.4 1st+Condon TVCF and Marcus rate constants for 121 MR-TADF molecules

Given that the Marcus predictions coincide closely with the experimental values for the above four molecules, checking the applicability of this error cancellation to other MR-TADF molecules would be interesting. Therefore, we extended the test set to 121 MR-TADF molecules [14], on which k_{RISC} calculations were performed at 1st+Condon and Marcus levels. Figs. 4**a**–4**c** show scatter plots comparing the calculated values and the experimental data. The rate constant equations were evaluated using $\Delta E_{\mathrm{ST}}^{(\mathrm{fit})}$, determined by the ARPSfit method. $\Delta E_{\mathrm{ST}}^{\mathrm{Exp}}$ was obtained from the RISC activation energy E_a^{Exp} based on the experimental Arrhenius plots or the difference between the measured fluorescence and phosphorescence photon energies [14] (Table S9).

Comparing Figs. 4**b** and 4**c** with their comparative plots in Fig. S6, we confirmed that the use of ARPSfit-based $\Delta E_{\mathrm{ST}}^{(\mathrm{fit})}$ showed better agreement with the experimental k_{RISC} than $\Delta E_{\mathrm{ST}}^{\mathrm{Exp}}$ for both models. The 1st+Condon model tended to underestimate k_{RISC} relative to the experimental data, with a Pearson correlation coefficient (PCC) of 0.51. This value favorably exceeded that of Marcus theory versus the experiments (0.33). However, there were several cases in which Marcus theory predicted a larger k_{RISC} than the 1st+Condon, resulting in a better agreement with the experimental measurements. This trend appeared to be related to the error cancellation observed in the previous analysis. However, in several instances, the Marcus results were significantly underestimated. Such large statistical variations in the Marcus results could be due to the Gaussian nature of the formula, which is sensitive to ΔE_{ST} alongside vibrational frequencies and reorganization energy. The underestimation of the 1st+Condon predictions may be rectified by the 2nd+HT treatment, which requires additional electronic structure computations.

Figs. 4**d**–4**f** show the plots of the Marcus and 1st+Condon results as a function of ΔE_{ST} for AZA-BN, BOBO-Z, and BN-CP2, respectively, as three typical classes. The reorganization energy λ plays a major role in determining the shape of the Marcus curve. In the large-λ case (e.g., AZA-BN) the ΔE_{ST}-dependent decay was as slow as that of the 1st+Condon model (Fig. 4**d**). The small-λ cases—BOBO-Z and BN-CP2—led the Marcus prediction to largely depend on ΔE_{ST} (Figs. 4**e** and 4**f**). A small ΔE_{ST} yielded a large k_{RISC} (BOBO-Z), and vice versa (BN-CP2). A notable feature could be observed in the Marcus results with small λ, ascribed to small structural changes between S_1 and T_1; for BN-CP2 (Type 3), the RISC transition was characterized as forbidden (Fig. 4**c**).

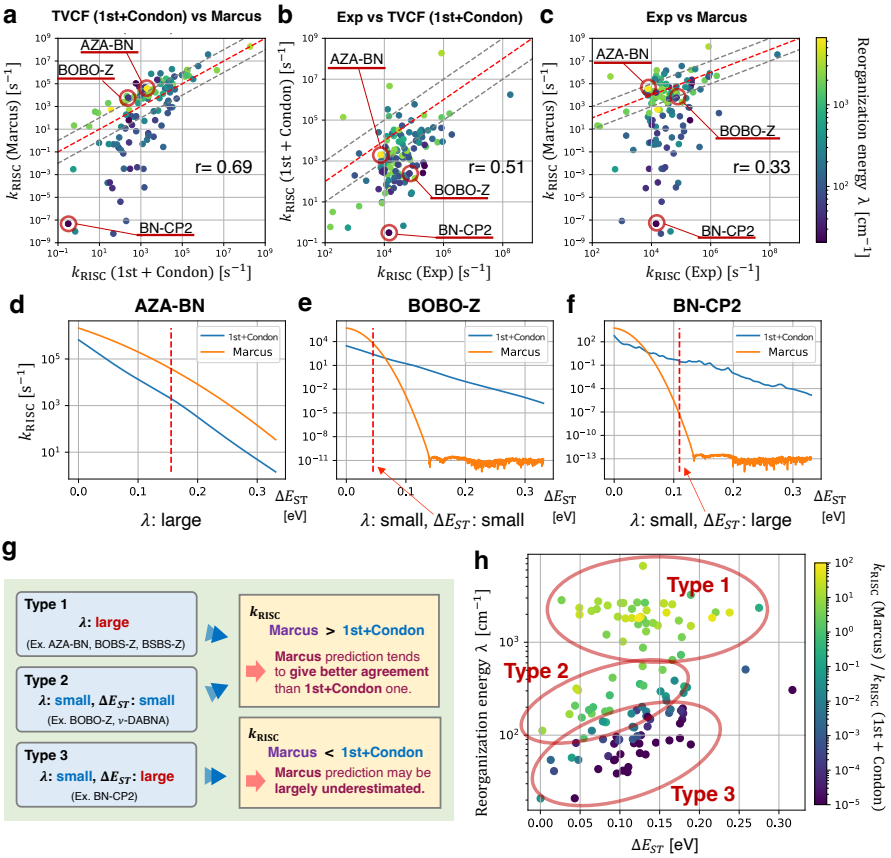

Fig. 4 **a,b,c,** Scatter plots to compare the experimental RISC rate constants k_{RISC} and the predicted rate constants using 1st+Condon and Marcus formulas with their parameter E_{ST} set to $\Delta E_{\mathrm{ST}}^{(\mathrm{fit})}$ for 121 MR-TADF molecules. The red dashed line indicates the exact agreement $y = x$. The two gray dashed lines indicate the relations $y = 0.1x$ and $y = 10x$. **d,e,f,** Plots of k_{RISC} as a function of ΔE_{ST} for AZA-BN (large λ), BOBO-Z (small λ and small ΔE_{ST}), and BN-CP2 (small λ and large ΔE_{ST}). **g,** The types of the MR-TADF molecules characteristics depending on ΔE_{ST} and λ: Types 1, 2, and 3. The magnitude relation between Marcus and 1st+Condon results depends on the type. **h,** Scatter plots of ΔE_{ST} versus reorganization energy λ for 121 MR-TADF molecules. The data points are classified into Types 1, 2, and 3, based on the ratio of k_{RISC} obtained by Marcus and 1st+Condon theories [k_{RISC}(Marcus)/k_{RISC}(1st+Condon)].

The above insights led us to classify the tested MR-TADF molecules into three types, depending on the degrees of ΔE_{ST} and λ. Fig. 4**g** summarizes these characteristics. Type 1 is associated with large λ, whereas Types 2 and 3 are associated with small λ. The ΔE_{ST} of Types 2 and 3 were characterized as small and large, respectively. Marcus theory tended to overestimate k_{RISC} for Types 1 and 2 and considerably underestimated k_{RISC} for Type 3 compared to the 1st-Condon estimations. However, the overestimation was prone to error

cancellation in the Marcus predictions, resulting in a near coincidence with the experimental k_{RISC}.

Fig. 4**h** shows scatter plots of λ versus ΔE_{ST} for 121 data points. Based on the ratio of k_{RISC}—Marcus versus 1st+Condon, these points appeared to fall into three categories, Types 1–3. Interestingly, this classification partitioned the data points approximately evenly. This implied that 30% of the Marcus predictions could be largely underestimated (Type 3). Meanwhile, the other 30% might suffer from erroneous overestimation but resulted in values closer to the experimental data (Type 1). This observation could also be confirmed in the cumulative histogram used to quantitatively analyze the distribution of the ratios relative to $k_{\mathrm{Exp.}}$ (Figs. S7 and S8).

3 Conclusions

We presented an in-depth analysis of the spin-flipping process of MR-TADF materials accelerated by two types of spin-vibronic interactions: NA-SVC and HT-SVC. The significance of their concerted effects, 2nd+HT, was identified as a factor that reliably characterized the RISC process. Full incorporation of the 2nd+HT terms into the TVCF framework was developed. This extended approach markedly outperformed the previous perturbative models. The accuracy of the predicted k_{RISC} is also susceptible to the precision of ΔE_{ST}. We developed the APRSfit method for effectively determining ΔE_{ST} based on the fitting to experimental Arrhenius plots. This method resulted in lower errors in the calculated k_{RISC}, compared with the cases using E_a^{Exp}.

Furthermore, we examined the extent to which each step of the approximation to the 1st+Condon theory, reduced to Marcus theory, affected k_{RISC} for MR-TADF systems. Our analyses indicate that the DHO and st approximations have a significant impact. These degradations cause fortuitous error cancellation in several Marcus results. By calculating k_{RISC} for 121 MR-TADF molecules, we identified the conditions that could closely align the Marcus predictions with the experimental values. One-third of the tested systems did not meet these conditions, and Marcus theory largely underestimated k_{RISC} for them.

Our extended modeling should benefit the reliable characterization of k_{RISC} for MR-TADF molecules despite its limitation by the harmonic approximation. Future work involves applying it to molecules underestimated by Marcus theory for molecular exploration.

Supplementary information. Supplementary Figs. S1–S8, Tables S1–S9, detailed derivation. Geometry data for the molecules considered.

Acknowledgments. This study was supported by JSPS KAKENHI (21H01881, JPJSBP120229601, JPJSBP120237705, and 22K21346 to T.Yan., 20K05430 to K.J.F., and 21H04694 to T.Yas.). T.Yas. and K.J.F. thank JST CREST (JPMJCR21O5). The authors thank Editage for English language editing.

References

[1] Tang, C.W., VanSlyke, S.A.: Organic electroluminescent diodes. Appl. Phys. Lett. **51**(12), 913–915 (1987). https://doi.org/10.1063/1.98799

[2] Burroughes, J.H., Bradley, D.D.C., Brown, A.R., Marks, R.N., Mackay, K., Friend, R.H., Burns, P.L., Holmes, A.B.: Light-emitting diodes based on conjugated polymers. Nature **347**(6293), 539–541 (1990). https://doi.org/10.1038/347539a0

[3] Friend, R.H., Gymer, R.W., Holmes, A.B., Burroughes, J.H., Marks, R.N., Taliani, C., Bradley, D.D.C., Santos, D.A.D., Brédas, J.L., Lögdlund, M., Salaneck, W.R.: Electroluminescence in conjugated polymers. Nature **397**(6715), 121–128 (1999). https://doi.org/10.1038/16393

[4] Baldo, M.A., O'Brien, D.F., You, Y., Shoustikov, A., Sibley, S., Thompson, M.E., Forrest, S.R.: Highly efficient phosphorescent emission from organic electroluminescent devices. Nature **395**(6698), 151–154 (1998). https://doi.org/10.1038/25954

[5] Adachi, C., Baldo, M.A., Thompson, M.E., Forrest, S.R.: Nearly 100% internal phosphorescence efficiency in an organic light-emitting device. J. Appl. Phys. **90**(10), 5048–5051 (2001). https://doi.org/10.1063/1.1409582

[6] Chen, Z., Qu, B., Luo, J., Kong, S., Gong, Q., et al.: Recent progresses on materials for electrophosphorescent organic light-emitting devices. Advanced (2011)

[7] Uoyama, H., Goushi, K., Shizu, K., Nomura, H., Adachi, C.: Highly efficient organic light-emitting diodes from delayed fluorescence. Nature **492**(7428), 234–238 (2012). https://doi.org/10.1038/nature11687

[8] Tao, Y., Yuan, K., Chen, T., Xu, P., Li, H., Chen, R., Zheng, C., Zhang, L., Huang, W.: Thermally activated delayed fluorescence materials towards the breakthrough of organoelectronics. Adv. Mater. **26**(47), 7931–7958 (2014). https://doi.org/10.1002/adma.201402532

[9] Wong, M.Y., Zysman-Colman, E.: Purely organic thermally activated delayed fluorescence materials for organic light-emitting diodes. Adv.

Mater. **29**(22) (2017). https://doi.org/10.1002/adma.201605444

[10] Nakanotani, H., Tsuchiya, Y., Adachi, C.: Thermally-activated delayed fluorescence for light-emitting devices. Chem. Lett. **50**(5), 938–948 (2021). https://doi.org/10.1246/cl.200915

[11] Hatakeyama, T., Shiren, K., Nakajima, K., Nomura, S., Nakatsuka, S., Kinoshita, K., Ni, J., Ono, Y., Ikuta, T.: Ultrapure blue thermally activated delayed fluorescence molecules: Efficient HOMO-LUMO separation by the multiple resonance effect. Adv. Mater. **28**(14), 2777–2781 (2016). https://doi.org/10.1002/adma.201505491

[12] Kothavale, S.S., Lee, J.Y.: Three- and four-coordinate, boron-based, thermally activated delayed fluorescent emitters. Adv. Opt. Mater. **8**(22), 2000922 (2020). https://doi.org/10.1002/adom.202000922

[13] Madayanad Suresh, S., Hall, D., Beljonne, D., Olivier, Y., Zysman-Colman, E.: Multiresonant thermally activated delayed fluorescence emitters based on heteroatom-doped nanographenes: Recent advances and prospects for organic light-emitting diodes. Adv. Funct. Mater. **30**(33), 1908677 (2020). https://doi.org/10.1002/adfm.201908677

[14] Kim, H.J., Yasuda, T.: Narrowband emissive thermally activated delayed fluorescence materials. Adv. Opt. Mater., 2201714 (2022). https://doi.org/10.1002/adom.202201714

[15] Marcus, R.A.: Electron transfer reactions in chemistry. theory and experiment. Rev. Mod. Phys. **65**(3), 599–610 (1993). https://doi.org/10.1103/RevModPhys.65.599

[16] Samanta, P.K., Kim, D., Coropceanu, V., Brédas, J.-L.: Up-Conversion Intersystem Crossing Rates in Organic Emitters for Thermally Activated Delayed Fluorescence: Impact of the Nature of Singlet vs Triplet Excited States. Journal of the American Chemical Society **139**(11), 4042–4051 (2017). https://doi.org/10.1021/jacs.6b12124

[17] Olivier, Y., Yurash, B., Muccioli, L., D'Avino, G., Mikhnenko, O., Sancho-García, J.C., Adachi, C., Nguyen, T.-Q., Beljonne, D.: Nature of the singlet and triplet excitations mediating thermally activated delayed fluorescence. Physical Review Materials **1**(7), 075602 (2017). https://doi.org/10.1103/PhysRevMaterials.1.075602

[18] Olivier, Y., Sancho-Garcia, J.-C., Muccioli, L., D'Avino, G., Beljonne, D.: Computational Design of Thermally Activated Delayed Fluorescence Materials: The Challenges Ahead. The Journal of Physical Chemistry Letters **9**(20), 6149–6163 (2018). https://doi.org/10.1021/acs.jpclett.8b02327

[19] Aizawa, N., Harabuchi, Y., Maeda, S., Pu, Y.-J.: Kinetic prediction of reverse intersystem crossing in organic donor–acceptor molecules. Nature Communications **11**(1), 3909 (2020). https://doi.org/10.1038/s41467-020-17777-2

[20] Penfold, T.J., Gindensperger, E., Daniel, C., Marian, C.M.: Spin-vibronic mechanism for intersystem crossing. Chem. Rev. **118**(15), 6975–7025 (2018). https://doi.org/10.1021/acs.chemrev.7b00617

[21] Peng, Q., Niu, Y., Shi, Q., Gao, X., Shuai, Z.: Correlation function formalism for triplet excited state decay: Combined Spin-Orbit and nonadiabatic couplings. J. Chem. Theory Comput. **9**(2), 1132–1143 (2013). https://doi.org/10.1021/ct300798t

[22] Northey, T., Penfold, T.J.: The intersystem crossing mechanism of an ultrapure blue organoboron emitter. Org. Electron. **59**, 45–48 (2018). https://doi.org/10.1016/j.orgel.2018.04.038

[23] Chen, X.-K., Zhang, S.-F., Fan, J.-X., Ren, A.-M.: Nature of highly efficient thermally activated delayed fluorescence in organic Light-Emitting diode emitters: Nonadiabatic effect between excited states. J. Phys. Chem. C **119**(18), 9728–9733 (2015). https://doi.org/10.1021/acs.jpcc.5b00276

[24] Peng, Q., Fan, D., Duan, R., Yi, Y., Niu, Y., Wang, D., Shuai, Z.: Theoretical study of conversion and decay processes of excited triplet and singlet states in a thermally activated delayed fluorescence molecule. J. Phys. Chem. C **121**(25), 13448–13456 (2017). https://doi.org/10.1021/acs.jpcc.7b00692

[25] Gibson, J., Monkman, A.P., Penfold, T.J.: The importance of vibronic coupling for efficient reverse intersystem crossing in thermally activated delayed fluorescence molecules. Chemphyschem **17**(19), 2956–2961 (2016). https://doi.org/10.1002/cphc.201600662

[26] Marian, C.M.: Spin-orbit coupling and intersystem crossing in molecules. Wiley Interdiscip. Rev. Comput. Mol. Sci. **2**(2), 187–203 (2012). https://doi.org/10.1002/wcms.83

[27] Tatchen, J., Gilka, N., Marian, C.M.: Intersystem crossing driven by vibronic spin-orbit coupling: a case study on psoralen. Phys. Chem. Chem. Phys. **9**(38), 5209–5221 (2007). https://doi.org/10.1039/B706410A

[28] Etinski, M., Tatchen, J., Marian, C.M.: Time-dependent approaches for the calculation of intersystem crossing rates. J. Chem. Phys. **134**(15), 154105 (2011). https://doi.org/10.1063/1.3575582

[29] Lin, S., Pei, Z., Zhang, B., Ma, H., Liang, W.: Vibronic coupling effect on the vibrationally resolved electronic spectra and intersystem crossing rates of a TADF emitter: 7-PhQAD. J. Phys. Chem. A **126**(2), 239–248 (2022). https://doi.org/10.1021/acs.jpca.1c08456

[30] Rodriguez-Serrano, A., Dinkelbach, F., Marian, C.M.: Intersystem crossing processes in the 2CzPN emitter: a DFT/MRCI study including vibrational spin–orbit interactions. Phys. Chem. Chem. Phys. **23**(5), 3668–3678 (2021). https://doi.org/10.1039/D0CP06011A

[31] Park, I.S., Matsuo, K., Aizawa, N., Yasuda, T.: High-performance dibenzoheteraborin-based thermally activated delayed fluorescence emitters: Molecular architectonics for concurrently achieving narrowband emission and efficient triplet-singlet spin conversion. Adv. Funct. Mater. **28**(34), 1802031 (2018). https://doi.org/10.1002/adfm.201802031

[32] Sun, H., Zhong, C., Brédas, J.-L.: Reliable prediction with tuned Range-Separated functionals of the Singlet–Triplet gap in organic emitters for thermally activated delayed fluorescence. J. Chem. Theory Comput. **11**(8), 3851–3858 (2015). https://doi.org/10.1021/acs.jctc.5b00431

[33] Kondo, M.: Singlet-triplet energy gap of multiresonant molecular systems: A double hybrid time-dependent density functional theory study. Chem. Phys. Lett. **804**, 139895 (2022). https://doi.org/10.1016/j.cplett.2022.139895

[34] Hall, D., Sancho-García, J.C., Pershin, A., Ricci, G., Beljonne, D., Zysman-Colman, E., Olivier, Y.: Modeling of multiresonant thermally activated delayed fluorescence emitters-properly accounting for electron correlation is key! J. Chem. Theory Comput. **18**(8), 4903–4918 (2022). https://doi.org/10.1021/acs.jctc.2c00141

[35] Niu, Y., Peng, Q., Deng, C., Gao, X., Shuai, Z.: Theory of excited state decays and optical spectra: application to polyatomic molecules. J. Phys. Chem. A **114**(30), 7817–7831 (2010). https://doi.org/10.1021/jp101568f

[36] Kondo, Y., Yoshiura, K., Kitera, S., Nishi, H., Oda, S., Gotoh, H., Sasada, Y., Yanai, M., Hatakeyama, T.: Narrowband deep-blue organic light-emitting diode featuring an organoboron-based emitter. Nat. Photonics **13**(10), 678–682 (2019)

[37] Park, I.S., Yang, M., Shibata, H., Amanokura, N., Yasuda, T.: Achieving ultimate narrowband and ultrapure blue organic light-emitting diodes based on polycyclo-heteraborin multi-resonance delayed-fluorescence emitters. Adv. Mater. **34**(9), 2107951 (2022). https://doi.org/10.1002/adma.202107951

[38] Lin, S.H., Chang, C.H., Liang, K.K., Chang, R., Shiu, Y.J., Zhang, J.M., Yang, T.-S., Hayashi, M., Hsu, F.C.: Ultrafast dynamics and spectroscopy of bacterial photosynthetic reaction centers. In: Advances in Chemical Physics. Advances in chemical physics, pp. 1–88. John Wiley & Sons, Inc., New York, USA (2002). https://doi.org/10.1002/0471264318.ch1

[39] Frisch, M.J., Trucks, G.W., Schlegel, H.B., Scuseria, G.E., Robb, M.A., Cheeseman, J.R., Scalmani, G., Barone, V., Petersson, G.A., Nakatsuji, H., Li, X., Caricato, M., Marenich, A.V., Bloino, J., Janesko, B.G., Gomperts, R., Mennucci, B., Hratchian, H.P., Ortiz, J.V., Izmaylov, A.F., Sonnenberg, J.L., Williams-Young, D., Ding, F., Lipparini, F., Egidi, F., Goings, J., Peng, B., Petrone, A., Henderson, T., Ranasinghe, D., Zakrzewski, V.G., Gao, J., Rega, N., Zheng, G., Liang, W., Hada, M., Ehara, M., Toyota, K., Fukuda, R., Hasegawa, J., Ishida, M., Nakajima, T., Honda, Y., Kitao, O., Nakai, H., Vreven, T., Throssell, K., Montgomery, J.A. Jr., Peralta, J.E., Ogliaro, F., Bearpark, M.J., Heyd, J.J., Brothers, E.N., Kudin, K.N., Staroverov, V.N., Keith, T.A., Kobayashi, R., Normand, J., Raghavachari, K., Rendell, A.P., Burant, J.C., Iyengar, S.S., Tomasi, J., Cossi, M., Millam, J.M., Klene, M., Adamo, C., Cammi, R., Ochterski, J.W., Martin, R.L., Morokuma, K., Farkas, O., Foresman, J.B., Fox, D.J.: Gaussian 16 Revision B.01. Gaussian Inc. Wallingford CT (2016)

[40] Epifanovsky, E., Gilbert, A.T.B., Feng, X., Lee, J., Mao, Y., Mardirossian, N., Pokhilko, P., White, A.F., Coons, M.P., Dempwolff, A.L., Gan, Z., Hait, D., Horn, P.R., Jacobson, L.D., Kaliman, I., Kussmann, J., Lange, A.W., Lao, K.U., Levine, D.S., Liu, J., McKenzie, S.C., Morrison, A.F., Nanda, K.D., Plasser, F., Rehn, D.R., Vidal, M.L., You, Z.-Q., Zhu, Y., Alam, B., Albrecht, B.J., Aldossary, A., Alguire, E., Andersen, J.H., Athavale, V., Barton, D., Begam, K., Behn, A., Bellonzi, N., Bernard, Y.A., Berquist, E.J., Burton, H.G.A., Carreras, A., Carter-Fenk, K., Chakraborty, R., Chien, A.D., Closser, K.D., Cofer-Shabica, V., Dasgupta, S., de Wergifosse, M., Deng, J., Diedenhofen, M., Do, H., Ehlert, S., Fang, P.-T., Fatehi, S., Feng, Q., Friedhoff, T., Gayvert, J., Ge, Q., Gidofalvi, G., Goldey, M., Gomes, J., González-Espinoza, C.E., Gulania, S., Gunina, A.O., Hanson-Heine, M.W.D., Harbach, P.H.P., Hauser, A., Herbst, M.F., Hernández Vera, M., Hodecker, M., Holden, Z.C., Houck, S., Huang, X., Hui, K., Huynh, B.C., Ivanov, M., Jász, Á., Ji, H., Jiang, H., Kaduk, B., Kähler, S., Khistyaev, K., Kim, J., Kis, G., Klunzinger, P., Koczor-Benda, Z., Koh, J.H., Kosenkov, D., Koulias, L., Kowalczyk, T., Krauter, C.M., Kue, K., Kunitsa, A., Kus, T., Ladjánszki, I., Landau, A., Lawler, K.V., Lefrancois, D., Lehtola, S., Li, R.R., Li, Y.-P., Liang, J., Liebenthal, M., Lin, H.-H., Lin, Y.-S., Liu, F., Liu, K.-Y., Loipersberger, M., Luenser, A., Manjanath, A., Manohar, P., Mansoor, E., Manzer, S.F., Mao, S.-P., Marenich, A.V., Markovich, T., Mason, S., Maurer, S.A., McLaughlin, P.F., Menger, M.F.S.J., Mewes, J.-M.,

Mewes, S.A., Morgante, P., Mullinax, J.W., Oosterbaan, K.J., Paran, G., Paul, A.C., Paul, S.K., Pavošević, F., Pei, Z., Prager, S., Proynov, E.I., Rák, Á., Ramos-Cordoba, E., Rana, B., Rask, A.E., Rettig, A., Richard, R.M., Rob, F., Rossomme, E., Scheele, T., Scheurer, M., Schneider, M., Sergueev, N., Sharada, S.M., Skomorowski, W., Small, D.W., Stein, C.J., Su, Y.-C., Sundstrom, E.J., Tao, Z., Thirman, J., Tornai, G.J., Tsuchimochi, T., Tubman, N.M., Veccham, S.P., Vydrov, O., Wenzel, J., Witte, J., Yamada, A., Yao, K., Yeganeh, S., Yost, S.R., Zech, A., Zhang, I.Y., Zhang, X., Zhang, Y., Zuev, D., Aspuru-Guzik, A., Bell, A.T., Besley, N.A., Bravaya, K.B., Brooks, B.R., Casanova, D., Chai, J.-D., Coriani, S., Cramer, C.J., Cserey, G., DePrince, A.E. 3rd, DiStasio, R.A. Jr, Dreuw, A., Dunietz, B.D., Furlani, T.R., Goddard, W.A. 3rd, Hammes-Schiffer, S., Head-Gordon, T., Hehre, W.J., Hsu, C.-P., Jagau, T.-C., Jung, Y., Klamt, A., Kong, J., Lambrecht, D.S., Liang, W., Mayhall, N.J., McCurdy, C.W., Neaton, J.B., Ochsenfeld, C., Parkhill, J.A., Peverati, R., Rassolov, V.A., Shao, Y., Slipchenko, L.V., Stauch, T., Steele, R.P., Subotnik, J.E., Thom, A.J.W., Tkatchenko, A., Truhlar, D.G., Van Voorhis, T., Wesolowski, T.A., Whaley, K.B., Woodcock, H.L. 3rd, Zimmerman, P.M., Faraji, S., Gill, P.M.W., Head-Gordon, M., Herbert, J.M., Krylov, A.I.: Software for the frontiers of quantum chemistry: An overview of developments in the Q-Chem 5 package. J. Chem. Phys. **155**(8), 084801 (2021). https://doi.org/10.1063/5.0055522

[41] Neese, F.: The ORCA program system. Wiley Interdiscip. Rev. Comput. Mol. Sci. **2**(1), 73–78 (2012). https://doi.org/10.1002/wcms.81

[42] Neese, F.: Software update: The ORCA program system—version 5.0. Wiley Interdiscip. Rev. Comput. Mol. Sci. **12**(5) (2022). https://doi.org/10.1002/wcms.1606

[43] Weigend, F.: Accurate coulomb-fitting basis sets for H to Rn. Phys. Chem. Chem. Phys. **8**(9), 1057–1065 (2006)

[44] Neese, F., Wennmohs, F., Hansen, A., Becker, U.: Efficient, approximate and parallel Hartree–Fock and hybrid DFT calculations. a 'chain-of-spheres' algorithm for the Hartree–Fock exchange. Chem. Phys. **356**(1-3), 98–109 (2009)

[45] Inai, N., Yamaguchi, S., Yanai, T.: Theoretical insight into the effect of phosphorus oxygenation on nonradiative decays: Comparative analysis of p-bridged stilbene analogs. ChemRxiv. Preprint. (2023). https://doi.org/10.26434/chemrxiv-2023-qv6d2

[46] Duschinsky, F.: The importance of the electron spectrum in multi atomic molecules. concerning the Franck-Condon principle. Acta Physicochim. URSS (1937)

[47] Avila Ferrer, F.J., Barone, V., Cappelli, C., Santoro, F.: Duschinsky, Herzberg–Teller, and multiple electronic resonance interferential effects in resonance raman spectra and excitation profiles. the case of pyrene. J. Chem. Theory Comput. **9**(8), 3597–3611 (2013). https://doi.org/10.1021/ct400197y

[48] Lee, M.H., Dunietz, B.D., Geva, E.: Calculation from first principles of intramolecular Golden-Rule rate constants for Photo-Induced electron transfer in molecular Donor-Acceptor systems. J. Phys. Chem. C **117**(44), 23391–23401 (2013). https://doi.org/10.1021/jp4081417

4 Methods

4.1 Computational details

The structural parameters of all the considered molecules were determined by performing TDDFT-level geometry optimizations for the S_1 and T_1 states separately. The TDDFT-level calculations, including the determination of vibrational states, were performed at the PBE0-D3BJ/def2-SV(P) level using Gaussian 16 [39]. This level was compatible with those employed in the precedent studies (e.g., Refs 16–18). The nonadiabatic coupling (NAC) matrix elements were calculated using Q-Chem version 5.4.2 [40]. The SOC matrix elements of the singlet and triplet states were evaluated at the PBE0/def2-SV(P) level using ORCA version 5.0.2 [41, 42]. For these SOC calculations, we used the SARC/J basis [43] for density fitting to the Coulomb term and the chain-of-sphere exchange (RIJCOSX) [44]. The derivatives of the SOC matrix elements were calculated *via* numerical differentiation of the T_1 structure.

All rate constants were calculated using an in-house code. The vibrational modes calculated at the initial and final states were used for the TVCF rate constant calculations, considering the Duschinsky rotation (for details, see Ref. 45). The correlation function was evaluated over a time range of 0.05 to 10 000.15 fs with a time step of 0.1 fs. The correlation function for the negative time was obtained from the complex conjugate of the positive time region. In the 2nd TVCF treatment, the T_2, T_3, and T_4 states were incorporated as intermediate states.

4.2 Formulation of 2nd+HT TVCF Theory

Let us here outline the formulation of the 2nd+HT TVCF rate constant equation. Sec. S7 in the supplementary information shows full details of the derivation. The 2nd+HT theory is built upon the second-order Fermi's golden rule given by

$$k_{f\leftarrow i} = \frac{2\pi}{\hbar}\sum_{v,u} P_{iv}\left|H'_{fu,iv} + \sum_{n,w}\frac{H'_{fu,nw}H'_{nw,iv}}{E_{iv}-E_{nw}}\right|^2 \delta(E_{iv}-E_{fu})\,. \tag{3}$$

which provides the transition rate between the initial (i) and final (f) states [38]. It is written using the vibronic state energies E_{iv} and E_{fu}, the Boltzmann distribution $P_{iv} = \frac{e^{-\beta E_{iv}}}{Z_i}$ with $Z_i = \sum_v e^{-\beta E_{iv}}$. We modeled the spin-flipping process using the perturbation $\hat{H}' = \hat{H}^{\mathrm{SOC}} + \hat{H}^{\mathrm{nBO}}$ consisting of the SOC term $\hat{H}^{\mathrm{SOC}}$ and the NAC term $\hat{H}^{\mathrm{nBO}} = \sum_k \hat{P}_{fk}^2$ with $\hat{P}_{fk} = -i\hbar\nabla_k$. The rate constants for the ISC and RISC transitions between S_1 and T_1 were evaluated as $k_{\mathrm{ISC}} = \sum_{m=0,\pm1} k_{\mathrm{T}_{1,m}\leftarrow \mathrm{S}_1}$ and $k_{\mathrm{RISC}} = \frac{1}{3}\sum_{m=0,\pm1} k_{\mathrm{S}_1\leftarrow \mathrm{T}_{1,m}}$,

respectively. As discussed in Sec. S7, equation (3) can be partitioned into the first- and second-order components as $k_{f\leftarrow i} = k^{\rm 1st}_{f\leftarrow i} + k^{\rm 2nd}_{f\leftarrow i}$, where $k^{\rm 1st}_{f\leftarrow i} = \frac{2\pi}{\hbar}\sum_{v,u} P_{iv}|H'_{fu,iv}|^2\delta(E_{iv} - E_{fu})$, which accounts for a direct transition process, and the rest, $k^{\rm 2nd}_{f\leftarrow i}$, is associated with an indirect process mediated by the intermediate states.

The SOC term was considered up to the Herzberg–Teller (HT) level [20], which describes $H^{\rm SOC}_{fu,iv}$ *via* the first-order Taylor expansion with respect to the vibration modes $\{Q_{fk}\}$ as $H^{\rm SOC}_{fu,iv} \simeq H^{\rm SOC}_{fi}\langle\Theta_{fu}|\Theta_{iv}\rangle + \sum_k \frac{\partial H^{\rm SOC}_{fi}}{\partial Q_{fk}}\langle\Theta_{fu}|Q_{fk}|\Theta_{iv}\rangle$, where the zeroth- and first-order terms are denoted Condon and HT, respectively. This form leads us to decompose $k^{\rm 1st}_{f\leftarrow i}$ and $k^{\rm 2nd}_{f\leftarrow i}$ further into the Condon and HT elements as $k^{\rm 1st}_{f\leftarrow i} = k^{\rm 1st,Condon}_{f\leftarrow i} + k^{\rm 1st,HT}_{f\leftarrow i}$ and $k^{\rm 2nd}_{f\leftarrow i} = k^{\rm 2nd,Condon}_{f\leftarrow i} + k^{\rm 2nd,HT}_{f\leftarrow i}$, respectively. By combining these elements, four levels of the rate-constant equation, the 1st+Condon, 1st+HT, 2nd+Condon, and 2nd+HT, are defined as follows:

$$k^{\rm 1st+Condon} = k^{\rm 1st,Condon}_{f\leftarrow i} \tag{4}$$

$$k^{\rm 1st+HT} = k^{\rm 1st,Condon}_{f\leftarrow i} + k^{\rm 1st,HT}_{f\leftarrow i} \tag{5}$$

$$k^{\rm 2nd+Condon} = k^{\rm 1st,Condon}_{f\leftarrow i} + k^{\rm 2nd,Condon}_{f\leftarrow i} \tag{6}$$

$$k^{\rm 2nd+HT} = k^{\rm 1st,Condon}_{f\leftarrow i} + k^{\rm 1st,HT}_{f\leftarrow i} + k^{\rm 2nd,Condon}_{f\leftarrow i} + k^{\rm 2nd,HT}_{f\leftarrow i} \tag{7}$$

These equations were evaluated within the framework of the thermal vibration correlation function (TVCF) method [21, 24]. In TVCF, the rate equation is expressed as a time-domain propagation of the normal-mode correlation function $\rho^{\rm (X)}_{fi}(t)$, as follows:

$$k^{\rm (X)}_{f\leftarrow i} = \frac{1}{\hbar^2}\int_{-\infty}^{\infty} dt\, e^{i\Delta E_{\rm ST}t/\hbar} Z_i^{-1}\rho^{\rm (X)}_{fi}(t)\,, \tag{8}$$

where X refers to the level of the formula: 1st+Condon, 1st+HT, 2nd+Condon, and 2nd+HT. Equation (8) is formed as a function of $\Delta E_{\rm ST}$ *via* the following identity:

$$\begin{aligned}\delta(E_{iv} - E_{fu}) &= \delta(\Delta E_{\rm ST} + E^i_v - E^f_u)\\ &= \frac{1}{2\pi}\int_{-\infty}^{\infty} d\tau\, e^{i\Delta E_{\rm ST}\tau} e^{i(E^i_v - E^f_u)\tau}\,,\end{aligned} \tag{9}$$

which is based on the relations $E_{iv} = E_i + E^i_v$, $E_{fu} = E_f + E^f_u$, and $\Delta E_{\rm ST} = E_i - E_f$, where E_i and E_f are the adiabatic electronic state energies, and E^i_v and E^f_u correspond to the vibrational state energies. Note that $\Delta E_{\rm ST}$ does not affect $\rho^{\rm (X)}_{fi}(t)$.

A major approximation in TVCF considers the molecular vibrations of each electronic state to be harmonic oscillations. This enables us to obtain an analytical formula for $\rho_{fi}^{(\mathrm{X})}(t)$ that can be evaluated in a computationally feasible manner. The resulting $\rho_{fi}^{(\mathrm{X})}(t)$ can be divided into X-independent and X-dependent factors as follows:

$$\rho_{fi}^{(\mathrm{X})}(t) = \rho_{fi}^{(\mathrm{core})}(t)\bar{\rho}_{fi}^{(\mathrm{X})}(t)\,. \tag{10}$$

The $\rho_{fi}^{(\mathrm{core})}(t)$ is given as

$$\rho_{fi}^{(\mathrm{core})}(t) = \sqrt{\frac{\det(\mathbf{a}\bar{\mathbf{a}})}{\det(\mathbf{D})}}\exp\left(\frac{i}{\hbar}\left[\mathbf{K}^{\mathbf{T}}\mathbf{C}\mathbf{K} - \frac{1}{2}\mathbf{E}^{\mathbf{T}}\mathbf{D}^{-\mathbf{1}}\mathbf{E}\right]\right)\,. \tag{11}$$

which is built upon various types of matrices defined as

$$\mathbf{A} \equiv \bar{\mathbf{a}} + \mathbf{J}^{\mathbf{T}}\mathbf{a}\mathbf{J} \tag{12}$$

$$\mathbf{B} \equiv \bar{\mathbf{b}} + \mathbf{J}^{\mathbf{T}}\mathbf{b}\mathbf{J} \tag{13}$$

$$\mathbf{C} \equiv \mathbf{b} - \mathbf{a} \tag{14}$$

$$\mathbf{D} \equiv \begin{bmatrix} \mathbf{B} & -\mathbf{A} \\ -\mathbf{A} & \mathbf{B} \end{bmatrix}_{2N_{\mathrm{vib}}\times 2N_{\mathrm{vib}}} \tag{15}$$

$$\mathbf{E} \equiv \begin{bmatrix} \mathbf{K}^{\mathsf{T}}\mathbf{C}\mathbf{J} \\ \mathbf{K}^{\mathsf{T}}\mathbf{C}\mathbf{J} \end{bmatrix}_{2N_{\mathrm{vib}}\times 1} \tag{16}$$

The $\mathbf{a}$ and $\mathbf{b}$ are diagonal matrices of the dimension N_{vib} with their elements $a_{jj} = \frac{\omega_j}{\hbar\sin(\omega_j t)}$ and $b_{jj} = \frac{\omega_j}{\hbar\tan(\omega_j t)}$ based on the initial state frequency ω_j. Their variants denoted $\bar{\mathbf{a}}$ and $\bar{\mathbf{b}}$, respectively, are based on the final state frequency $\bar{\omega}_j$ in the place of ω_j. $\mathbf{J}$ is the Duschinsky rotation matrix [46, 47] and $\mathbf{K}$ is the displacement vector between the initial and final states.

The integral in equation (8) can be evaluated using the Fourier transform of $\rho_{fi}^{(\mathrm{X})}(t)$ from the time (t) domain to the energy (ΔE_{ST}) domain, where $\rho_{fi}^{(\mathrm{X})}(t)$ [equation (10)] is evaluated at grid points of $t \in [-t_{\max}, t_{\max}]$. The resulting $k_{f\leftarrow i}$ is obtained as a function of ΔE_{ST}, which is represented on a grid in energy coordinates. The objective $k_{f\leftarrow i}$ can be determined by substituting ΔE_{ST} with the user-input value of the adiabatic energy difference, ΔE_{fi}.

4.3 Comparison of the 1st+Condon TVCF method and Marcus formula

In previous studies, the semi-classical Marcus formula [15] was mostly employed to calculate the RISC rate constants, as follows:

$$k_{\mathrm{RISC}}^{\mathrm{Marcus}}(\Delta E_{\mathrm{ST}}) = \frac{2\pi}{\hbar}|H_{fi}^{\mathrm{SOC}}|^2 \frac{1}{\sqrt{4\pi\lambda_{\mathrm{RISC}} k_{\mathrm{B}} T}} \exp\left(\frac{-E_a^{\mathrm{RISC}}}{k_{\mathrm{B}} T}\right) \tag{17}$$

where λ_{RISC} is the reorganization energy, and E_a^{RISC} is defined as:

$$E_a^{\mathrm{RISC}} = \frac{(\Delta E_{\mathrm{ST}} + \lambda_{\mathrm{RISC}})^2}{4\lambda_{\mathrm{RISC}}}\,. \tag{18}$$

The Marcus equation can be derived from the 1st+Condon equation $k^{\mathrm{1st+Condon}}$ [equation (4)], *via* stepwise approximations [38, 48].

Equation (4) is re-written as

$$k_{f\leftarrow i}^{\mathrm{1st+Condon}}(\Delta E_{\mathrm{ST}}) = \frac{\left|H_{fi}^{\mathrm{SOC}}\right|^2}{\hbar^2} \int_{-\infty}^{\infty} dt\, e^{i\Delta E_{\mathrm{ST}}\, t/\hbar}\, Z_i^{-1} \rho^{\mathrm{1st+Condon}}(t)\,, \tag{19a}$$

$$\rho^{\mathrm{1st+Condon}}(t) = \sqrt{\frac{\det(\mathbf{a\bar{a}})}{\det(\mathbf{D})}} \exp\left(\frac{i}{\hbar}\left[\mathbf{K^T C K} - \frac{1}{2}\mathbf{E^T D^{-1} E}\right]\right), \tag{19b}$$

The initial step to approximate $k_{f\leftarrow i}^{\mathrm{1st+Condon}}$ toward Marcus theory is to cut off the Duschinsky rotation by setting $\mathbf{J}$ to an identity matrix (Dus-off). This enables $\rho(t)$ to be factorized into separate entities associated with each vibrational mode, as follows:

$$\begin{aligned} Z_i^{-1}\rho^{\mathrm{Dus\text{-}off}}(t) = \prod_j^N \Bigg[& \left(\frac{\omega_j \bar{\omega}_j}{\sin(\omega_j t_i)\sin(\bar{\omega}_j t_f)}\right) \\ & \left(\omega_j \cot\left(\frac{\omega_j t_i}{2}\right) + \bar{\omega}_j \cot\left(\frac{\bar{\omega}_j t_f}{2}\right)\right)^{-1} \\ & \left(-\omega_j \tan\left(\frac{\omega_j t_i}{2}\right) - \bar{\omega}_j \tan\left(\frac{\bar{\omega}_j t_f}{2}\right)\right)^{-1}\Bigg]^{\frac{1}{2}} \\ & \times \exp\left(-iK_j^2 \frac{\omega_j \bar{\omega}_j}{\omega_j \cot\frac{\bar{\omega}_j t_f}{2} + \bar{\omega}_j \cot\frac{\omega_j t_i}{2}}\right) \end{aligned} \tag{20}$$

Furthermore, we consider the displaced harmonic oscillator (DHO) model, which uses the common frequency for the initial-state ω_j and the final-state

$\bar{\omega}_j$, resulting in

$$Z_i^{-1}\rho^{\mathrm{DHO}}(t) = \prod_j^N \exp\left\{ -S_j\Big[(1+2\bar{n}_j) - (1+\bar{n}_j)\exp(-i\omega_j t) - \bar{n}_j \exp(i\omega_j t)\Big]\right\} \tag{21}$$

where $S_j \equiv \frac{K_j^2\omega_j}{2\hbar}$ and $\bar{n}_j \equiv \frac{1}{\exp(\hbar\beta\omega_j)-1}$. The short-time (st) approximation, $\exp(\pm i\omega_j t) \simeq 1 \pm i\omega_j t - \frac{1}{2}\omega_j^2 t^2$, subject to the assumption $\omega_j t \ll 1$, is applied to equation (21), which results in

$$Z_i^{-1}\rho^{\mathrm{st}}(t) = \exp\left\{-i\sum_j^N S_j\omega_j t - \sum_j \left(S_j\bar{n}_j + \frac{1}{2}\right)\omega_j^2 t^2\right\} \tag{22}$$

Finally, the Marcus equation [equation (17)] can be derived using equation (22) by applying the high-temperature (ht) approximation that the temperature T is sufficiently large and $\hbar\omega_j/kT \ll 1$ holds.

$$Z_i^{-1}\rho^{\mathrm{Marcus}}(t) = \exp\left\{-i\sum_j^N S_j\omega_j t - \sum_j S_j\bar{n}_j\omega_j^2 t^2\right\} \tag{23}$$

Abbreviation List

MR	Multi-resonance
TADF	Thermally activated delayed fluorescence
ISC	Intersystem crossing
RISC	Reverse intersystem crossing
TVCF	Thermal vibration correlation function
HT	Herzberg–Teller approximation
SOC	Spin-orbit coupling
SVC	Spin-vibronic coupling
NAC	Non-adiabatic coupling
TDDFT	Time-dependent density-functional theory
SCS-CC2	Spin-component-scaled second-order approximate coupled-cluster singles and doubles
Dus	Dushcinsky rotation
DHO	Displaced harmonic oscillator approximation
st	Short-time approximation
ht	High-temperature approximation